Orthogonal Magnetization and Symmetry Breaking in Pyrochlore Iridate $Eu_2Ir_2O_7$

Tian Liang[1,*], Timothy H. Hsieh[2,*,†], Jun J. Ishikawa[3], Satoru Nakatsuji[3,4], Liang Fu[2] and N. P. Ong[1]
[1]*Department of Physics, Princeton University, Princeton, NJ 08544*
[2]*Department of Physics, Massachusetts Institute of Technology, Cambridge, MA 02139*
[3]*Institute for Solid State Physics, University of Tokyo, Kashiwa 277-8581, Japan*
[4]*PRESTO, Japan Science and Technology Agency (JST), 4-1-8 Honcho Kawaguchi, Saitama 332-0012, Japan*
(Dated: March 29, 2016)

arXiv:1603.08022v1 [cond-mat.str-el] 25 Mar 2016

Electrons in the pyrochore iridates experience a large interaction energy in addition to a strong spin-orbit interaction. Both features make the iridates promising platforms for realizing novel states such as the Topological Mott Insulator. A further ingredient in pyrochlores is geometric frustration which leads to unusual magnetic states. The pyrochlore $Eu_2Ir_2O_7$ exhibits a ground state consistent with the all-in, all-out (AIAO) state. Using torque magnetometry, we uncover a highly unusual magnetic response in agreement with AIAO predictions. A magnetic field H applied in its a-b plane produces a nonlinear magnetization $M_\perp$ orthogonal to the plane. $M_\perp$ displays a d-wave field-angle pattern consistent with octupole order, with a handedness (chirality ω) dictated by field cooling, leading to symmetry breaking of chirality. A surprise is that the lobe orientation of the d-wave pattern is sensitive to the direction of the field when the sample is field-cooled below T_N, suggestive of an additional order parameter η already present at 300 K.

An expanding area of research on topological matter is exploring the role of interactions. Theory predicts that when the interaction energy U and spin orbit interaction (SOI) λ are both large, an exotic state, the Topological Mott Insulator (TMI) which features gapless surface spin-only excitations, is stable [1, 2]. As λ decreases (with U still large), a transition occurs from the TMI to a semimetal state with topologically protected Weyl nodes [3–7]. The pyrochlore iridates, comprised of networks of vertex sharing tetrahedra [1, 8], have emerged as likely materials for realizing these novel states.

At each Ir^{4+} site, the five $5d$ electrons occupy the 6 t_{2g} orbitals derived from d_{xy}, d_{yz} and d_{zx} states (crystal field splitting lifts the e_g orbitals high above the t_{2g} manifold). The large SOI splits the t_{2g} manifold into a $J = \frac{1}{2}$ doublet with energy λ and a $J = \frac{3}{2}$ quadruplet with energy $-\lambda/2$ [2, 9, 10]. At the critical temperature $T_N \sim 120$ K, $Eu_2Ir_2O_7$ undergoes a transition to an insulating state (Fig. 1A) [11–14]. Resonant x-ray scattering reveals that the ordering vector $\mathbf{q} = 0$. Together with the absence of a structural phase transition at T_N, the x-ray evidence suggests that the insulating state has the all-in/all-out (AIAO) magnetic configuration in which the spins at the vertices of a tetrahedron either all point in or out [15–22] [Figs. S1 and S2 in Supplementary Information (SI)]. In $Nd_2Ir_2O_7$, the ordered state of Nd was also argued to be AIAO from neutron scattering experiments [19].

Although symmetry arguments predict that the magnetization in the AIAO state should be very interesting, no experiments have been reported. The ordered state of pyrochlore iridates has zero net magnetic moment (the sum of dipoles cancel to zero in the tetrahedra). Moreover, the quadrapole term vanishes because of inversion symmetry [23, 24]. Hence it is necessary to consider octupolar order for which the susceptibility is a third-rank tensor ω_{ijk} (i, j, k refer to components along the unit cell vectors **a**, **b**, **c**). In the AIAO state, the only nonzero tensor elements are ω_{312} and its 5 permutations. They are all equal to the chirality ω which equals +1 in the AIAO state, and -1 in the time-reversed partner state (see Sec. S1 and Figs. S1 and S2 in SI). This leads to the interesting prediction that a field $\mathbf{H} = (H_a, H_b, 0)$ confined to the a-b plane produces a nonlinear magnetization $\mathbf{M}_\perp$ normal to the plane, viz.

$$M_\perp = \omega \chi_\perp H_a H_b, \tag{1}$$

where the susceptibility $\chi_\perp(T)$ describes its T dependence.

We emphasize that the direction of $\mathbf{M}_\perp$ (which we call orthogonal magnetization) cannot be inferred *a priori* from the signs of H_a and H_b. By necessity, its appearance spontaneously breaks a Z_2 symmetry (the system spontaneously chooses ω to be either +1 or -1). We contrast it with the trivial case in which a tilted **H** can tilt a magnetization vector away from its easy plane when the anisotropy field is exceeded. The induced normal component $\mathbf{M}_{trans}$, previously called "transverse" magnetization [25, 26], does not involve breaking of a Z_2 symmetry ($\mathbf{M}_{trans}$ just comes from the spin canting via ordinary Zeeman coupling to **H**) (see sec. S6 in SI for more discussion).

In our set-up, it is convenient to define the (lab) x and y axes as rotated by 45° relative to the lattice vectors **a** and **b** of the pyrochlore unit cell [$\hat{\mathbf{x}} \parallel (1\bar{1}0)$, $\hat{\mathbf{y}} \parallel (110)$ and $\hat{\mathbf{z}} \parallel (001)$] (Fig. 1B). The axis of the torque cantilever is aligned $\parallel \hat{\mathbf{x}}$. With **H** in the a-b plane (at an angle φ to $\hat{\mathbf{y}}$), the torque signal is given by $\tau = M_z H_y$ – the torque detects the magnetization component M_z normal to the plane in which **H** lies (Supplementary Figs. S2 and S3).

In $Eu_2Ir_2O_7$, M_z consists of three terms $M_s \propto H^0$, $M_p \propto H$, $M_\perp \propto H^2$, viz. $M_z = M_s + M_p + M_\perp$. Accordingly, the observed torque (with φ and T fixed) can

be represented as

$$\tau \equiv \tau_s + \tau_p + \tau_\perp = \alpha H + \beta H^2 + \gamma H^3. \qquad (2)$$

(We refer to the H-even and H-odd parts as $\tau_{even} \equiv \tau_p = \beta H^2$ and $\tau_{odd} \equiv \tau_s + \tau_\perp = \alpha H + \gamma H^3$, respectively.) The first term αH corresponds to a field independent magnetization $M_s \equiv \alpha/\cos\varphi$. The second term τ_{even} – the largest term in our field range – comes from a paramagnetic magnetization $M_p \equiv \beta H/\cos\varphi$. In contrast to M_s, M_p which persist up to 300 K (see below and SI), the third term γH^3, which onsets below T_N = 120 K, corresponds to the orthogonal magnetization $M_\perp \equiv \gamma H^2/\cos\varphi$, coming from the octupole order.

By antisymmetrization, we can isolate τ_{odd}, which we plot in Fig. 1C at 5 K (Supplementary Sec. S4 and Fig. S3). The plot clearly shows the H^3 variation produced by $M_\perp$ (plus a term from M_s). Dividing by H, we then isolate $M_\perp$ as a parabola resting on a constant term M_s (Fig. 1D). We note that the sign, sgn(M_s), inverts between sweep-up and -down curves as expected. However, sgn($M_\perp$) and its absolute value (namely, the curvature of the parabola) stay the same, implying the different origin between $M_\perp$ and M_s (as well as M_p, see SI for more information). The striking rigidity of sgn($M_\perp$) implies an unusual domain-wall feature of the octupole order. The procedure is repeated over selected angles $0 < \varphi < 360°$ to isolate the T dependence of $M_\perp$ from 5 K to 300 K.

First, we examine the angular variation of $M_\perp$ at 5 K. As shown in Fig. 2A, the curve of $\tau_\perp = M_\perp H\cos\varphi$ vs. φ. The angular variation is nominally described by the red curve representing a d-wave form $\cos 2\varphi$ (Panel B), viz.

$$M_\perp(T,\varphi) = \chi_\perp(T)H^2(1+\eta\cos\varphi)\cos 2\varphi, \qquad (3)$$

where the "orthogonal" susceptibility $\chi_\perp(T)$ grows like an order parameter below T_N. The observation of an orthogonal magnetization varying as H^2 with a d-wave pattern, as predicted in Eq. 1, constitutes strong evidence for the AIAO magnetic octupole order. The parameter η, which distorts the d-wave pattern, is a phenomenological term which represents additional order which already exists at 300 K (see below and SI). The results in Fig. 2A were measured after field-cooling in the (9 T) field $\mathbf{H}_{fc} \parallel -\hat{\mathbf{y}}$. We find that $M_\perp$ changes in sign if $\mathbf{H}_{fc}$ is inverted. We identify the chirality $\omega = 1$ if $\mathbf{H}_{fc} \parallel -\hat{\mathbf{y}}$ (and -1 if $\mathbf{H}_{fc} \parallel \hat{\mathbf{y}}$). See Supplementary Sec. S5 and Fig. S4. This symmetry breaking of the chirality sharply distinguishes the octupolar nature of $M_\perp$ from transverse magnetization $\mathbf{M}_{trans}$ whose origin is strictly dipolar.

Further evidence for the octupolar origin of $M_\perp$ derives from the hysteresis behavior of the domain walls (DWs) vs. T. In conventional dipolar magnets, $\mathbf{H}$ exerts a strong force on the DW because of dipolar coupling. By contrast, for the DW between octupolar domains, a much weaker force is expected. We next describe evidence that the DWs for $M_\perp$ are virtually immobile at low T. As already noted in Fig. 1D, sgn($M_\perp$) is "frozen", unlike sgn(M_s). As T is raised above 25 K, the reversibility gives way to a large hysteresis. At 60 K, $\tau_\perp$ is strongly hysteretic (Figs. 3A and 3B show the hysteresis observed for the two d-wave patterns attained with different $\mathbf{H}_{fc}$). In Figs. 3C and 3D, we plot the T dependence of $M_\perp$ measured in up-sweep (red circles) and down-sweep traces (blue) from 5 K to 150 K with φ fixed at the lobe maxima.

A striking pattern is that the difference between the red and blue curves (the "hysteresis amplitude" $\Delta M_\perp$) is largest near 75 K, but rapidly decreases to below resolution for $T < 25$ K. This decrease fits well to the thermal activation form $e^{-\Delta/T}$ with Δ = 170 and 220 K in C and D, respectively (Supplementary Fig. S6). At each T, $\Delta M_\perp$ measures the distance of DW diffusion on our timescales (sweep rates of 1 T/min). Hence the activated form implies diffusion times that grow exponentially with decreasing T. The activated form explains why sgn($M_\perp$) is frozen at 5 K in Fig. 1D. Once a domain pattern is established at 5 K, it is very difficult to erase the pattern because the DWs are immobile on experimental timescales. Both the activated form and the frozen configuration at 5 K reflect the weak coupling of octupolar DWs to $\mathbf{H}$. By contrast, the field independent term M_s has a very different hysteretic behavior vs. T (see Supplementary Fig. S4).

An unexpected finding is that the angular orientation of the d-wave lobes can be rotated by cooling in a field $\mathbf{H}_{fc}$ parallel to $-\hat{\mathbf{x}}$, breaking the underlying lattice symmetry between two "equivalent" axes x-axis and y-axis (the system is cubic). Cooling to 5 K in the new $\mathbf{H}_{fc}$ leads to the plot of $M_\perp$ shown in Fig. 2C. The d-wave pattern (with $\omega = 1$) is now shifted by 45° (Fig. 2D) and described by

$$M_\perp(T,\varphi) = \chi_\perp(T)H^2(1+\eta\cos\varphi)\sin 2\varphi. \qquad (4)$$

Here, η is again the phenomenological term representing the additional order that already exists at 300 K (see below and SI). We have also explored cooling with $\mathbf{H}_{fc}$ in other directions. When cooled in say $\mathbf{H}_{fc} \parallel \mathbf{a}$, the observed $M_\perp$ vs. φ is a linear combination of the two d-wave pattern discussed above. Hence we infer that the two principal axes for field cooling are $\hat{\mathbf{x}} \parallel (1\bar{1}0)$ and $\hat{\mathbf{y}} \parallel (110)$ ($\hat{\mathbf{y}}$ is identified later as the axis favored by η). See Supplementary Fig. S5.

The breaking of the underlying C_4 lattice symmetry implies that an additional order exists above T_N. A first clue comes from the existence of M_s above T_N = 120 K. Figure S10 (SI) shows the angular dependence of τ_s and $\tau_\perp$ at 150 K. While τ_s (hence M_s) remains finite at 150 K and retains the same angular pattern seen at 5 K (see Fig. S5 in SI), $\tau_\perp$ (hence $M_\perp$) vanishes completely. The differences imply that M_s and $M_\perp$ are associated with very different magnetic ordering.

To investigate this additional order, we examine the paramagnetic term M_p which is strictly H-linear, with an angular variation that remains unchanged from 5 to 300 K. Figure 4A plots τ_{even} ($= \tau_p$) versus φ at T =

5, 150 and 300 K. The sinusoidal variation has the distorted dipolar form (inset) that fits well to the expression $(M_p/H)\cos\varphi$, where M_p has the form

$$M_p(T,\varphi) = \chi_p(T)H(1+\eta\cos\varphi)\cos\varphi. \quad (5)$$

All its T dependence resides in the amplitude $\chi_p(T)$ (Fig. 4B). The parameter η (nearly T independent) represents the additional order that develops along y-axis, breaking the underlying C_4 lattice symmetry (see SI for further discussion of the η term).

The symmetry breaking of handedness (chirality) together with the activated behavior of DWs of $M_\perp$ sharply distinguishes octupolar from dipolar order. The existence of the additional order parameter η which already exists at 300 K allows the system to assume two different d-wave lobe patterns of $M_\perp$. Exploring the mechanism of symmetry breaking of handedness in octupole order, namely, what is the conjugate of the octupole order parameter, as well as the origin of additional order η are fruitful directions to pursue in the iridates.

[1] Pesin, D. & Balents, L. Mott physics and band topology in materials with strong spin-orbit interaction. *Nature Phys.* **6**, 376–381 (2010).

[2] Witczak-Krempa, W., Chen, G., Kim, Y. B. & Balents, L. Correlated quantum phenomena in the strong spin-orbit regime. *Annual Review of Condensed Matter Physics* **5**, 57–82 (2014).

[3] Wan, X., Turner, A. M., Vishwanath, A. & Savrasov, S. Y. Topological semimetal and Fermi-arc surface states in the electronic structure of pyrochlore iridates. *Phys. Rev. B* **83**, 205101 (2011).

[4] Turner, A. M. & Vishwanath, A. Beyond Band Insulators: Topology of Semi-metals and Interacting Phases. *ArXiv e-prints* (2013). 1301.0330.

[5] Witczak-Krempa, W., Chen, G., Kim, Y. B. & Balents, L. Correlated Quantum Phenomena in the Strong Spin-Orbit Regime. *Annu. Rev. Condens* **5**, 57–82 (2014).

[6] Witczak-Krempa, W. & Kim, Y. B. Topological and magnetic phases of interacting electrons in the pyrochlore iridates. *Phys. Rev. B* **85**, 045124 (2012).

[7] Savary, L., Moon, E.-G. & Balents, L. New Type of Quantum Criticality in the Pyrochlore Iridates. *Phys. Rev. X* **4**, 041027 (2014).

[8] Jackeli, G. & Khaliullin, G. Mott Insulators in the Strong Spin-Orbit Coupling Limit: From Heisenberg to a Quantum Compass and Kitaev Models. *Phys. Rev. Lett.* **102**, 017205 (2009).

[9] Kim, B. J. *et al.* Novel $J_{\rm eff} = 1/2$ Mott State Induced by Relativistic Spin-Orbit Coupling in Sr_2IrO_4. *Phys. Rev. Lett.* **101**, 076402 (2008).

[10] Kim, B. J. *et al.* Phase-Sensitive Observation of a Spin-Orbital Mott State in Sr_2IrO_4. *Science* **323**, 1329–1332 (2009).

[11] Matsuhira, K. *et al.* Metal-Insulator Transition in Pyrochlore Iridates $Ln_2Ir_2O_7$ (Ln = Nd, Sm, and Eu). *J. Phys. Soc. Jpn* **76**, 043706 (2007).

[12] Matsuhira, K., Wakeshima, M., Hinatsu, Y. & Takagi, S. Metal-insulator Transitions in Pyrochlore Oxides $Ln_2Ir_2O_7$. *Journal of the Physical Society of Japan* **80**, 094701 (2011).

[13] Ishikawa, J. J., O'Farrell, E. C. T. & Nakatsuji, S. Continuous transition between antiferromagnetic insulator and paramagnetic metal in the pyrochlore iridate $Eu_2Ir_2O_7$. *Phys. Rev. B* **85**, 245109 (2012).

[14] Tafti, F. F., Ishikawa, J. J., McCollam, A., Nakatsuji, S. & Julian, S. R. Pressure-tuned insulator to metal transition in $Eu_2Ir_2O_7$. *Phys. Rev. B* **85**, 205104 (2012).

[15] Sagayama, H. *et al.* Determination of long-range all-in-all-out ordering of Ir^{4+} moments in a pyrochlore iridate $Eu_2Ir_2O_7$ by resonant x-ray diffraction. *Phys. Rev. B* **87**, 100403 (2013).

[16] Yo Machida, Satoru Nakatsuji, Shigeki Onoda, Takashi Tayama and Toshiro Sakakibara, "Time-reversal symmetry breaking and spontaneous Hall effect without magnetic dipole order," Nature **463**, 210-213 (2010).

[17] Zhao, S. *et al.* Magnetic transition, long-range order, and moment fluctuations in the pyrochlore iridate $Eu_2Ir_2O_7$. *Phys. Rev. B* **83**, 180402 (2011).

[18] Yamaura, J. *et al.* Tetrahedral Magnetic Order and the Metal-Insulator Transition in the Pyrochlore Lattice of $Cd_2Os_2O_7$. *Phys. Rev. Lett.* **108**, 247205 (2012).

[19] Tomiyasu, K. *et al.* Emergence of Magnetic Long-range Order in Frustrated Pyrochlore $Nd_2Ir_2O_7$ with Metal-Insulator Transition. *J. Phys. Soc. Jpn* **81**, 034709 (2012).

[20] Ueda, K. *et al.* Variation of Charge Dynamics in the Course of Metal-Insulator Transition for Pyrochlore-Type $Nd_2Ir_2O_7$. *Phys. Rev. Lett.* **109**, 136402 (2012).

[21] Ueda, K. *et al.* Anomalous domain-wall conductance in pyrochlore-type $Nd_2Ir_2O_7$ on the verge of the metal-insulator transition. *Phys. Rev. B* **89**, 075127 (2014).

[22] Ma, E. Y. *et al.* Mobile metallic domain walls in an all-in-all-out magnetic insulator. *Science* **350**, 538 (2015).

[23] Santini, P. *et al.* Multipolar interactions in f-electron systems: The paradigm of actinide dioxides. *Rev. Mod. Phys.* **81**, 807–863 (2009).

[24] Kuramoto, Y., Kusunose, H. & Kiss, A. Multipole Orders and Fluctuations in Strongly Correlated Electron Systems. *Journal of the Physical Society of Japan* **78**, 072001 (2009).

[25] Glazkov, V. N. *et al.* Single-ion anisotropy in the gadolinium pyrochlores studied by electron paramagnetic resonance. *Phys. Rev. B* **72**, 020409 (2005).

[26] Glazkov, V. N., Marin, C. & Sanchez, J.-P. Observation of a transverse magnetization in the ordered phases of the pyrochlore magnet $Gd_2Ti_2O_7$. *J. Phys. Condens. Matter* **18**, L429–L434 (2006).

*These authors contributed equally to this work.

†Current address of T.T.H.: Kavli Institute for Theoretical Physics, University of California, Santa Barbara, CA 93106

Supplementary Information is available in the online version of the paper.

Acknowledgements T.L. acknowledges a scholarship from Japan Student Services Organization. L.F. and T.H. were supported by DOE Office of Basic Energy Sciences, de-sc0010526. T.H. thanks the KITP graduate fellowship program. The research at Univ. Tokyo is supported by grants-in-aid (nos. 25707030) and the Program for Advancing Strategic International Networks to Accelerate the Circulation of Talented Researchers (no. R2604) from JSPS, by PRESTO to JST, and grant-in-aid for scientific research on Innovative Areas (Grants No. 15H05882 and No. 15H05883) from MEXT. N.P.O. acknowledges the support of the U.S. National Science Foundation (Grant DMR 1420541) and the Gordon and Betty Moore Foundations EPiQS Initiative through Grant GBMF4539.

Author Contributions T.L., T.T.H., L. F. and N.P.O. conceived the idea behind the experiment. T.L. designed the experiment and carried out all the measurements. T.L. and N.P.O. analyzed the results with important insights from T.T.H. and L.F. The manuscript was written by T.L. and N.P.O. with numerous inputs from T.T.H. and L.F. The crystal was grown by J.J.I. and S.N.

Author Information The authors declare no competing financial interests. Correspondence and requests for materials should be addressed to T.L. (tliang@princeton.edu) and N.P.O. (npo@princeton.edu).

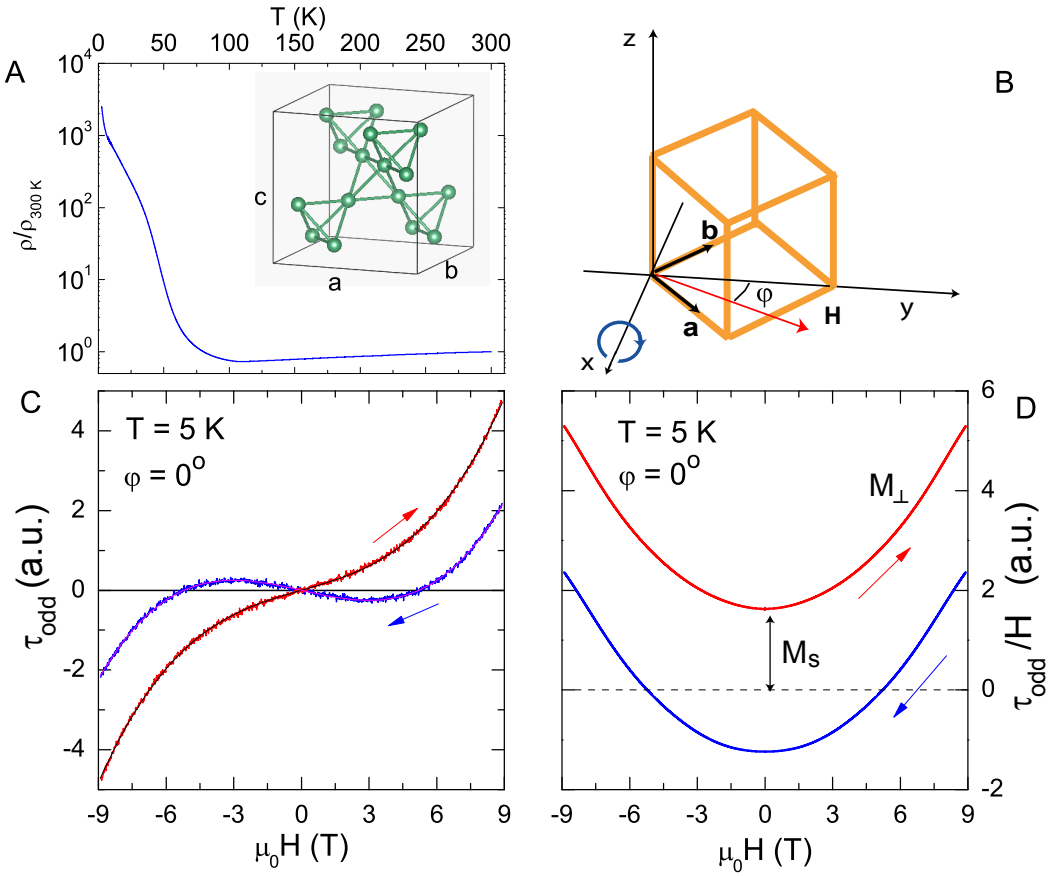

FIG. 1: The pyrochlore lattice, orientation of the lab axes, and analysis of the torque signal. Panel A shows the lattice of the pyrochlore $Eu_2Ir_2O_7$. A sketch of the orientation of the lab frame $\hat{\mathbf{x}}$, $\hat{\mathbf{y}}$ and $\hat{\mathbf{z}}$ relative to the lattice vectors **a**, **b** and **c** is shown in Panel B. The axis of the torque cantilever is parallel to $\hat{\mathbf{x}}$ as indicated by the blue circle. With **H** (red arrow) in the a-b plane at an angle φ to $\hat{\mathbf{y}}$, the torque component detected is $\tau_x = M_z H \cos\varphi$. Panel C plots the H-odd component of the torque τ_{odd} (see Eq. 2) measured in field sweep-up (-9 → 9 T, red) and sweep-down (9 →-9 T, blue) scans at 5 K and angle $\varphi = 0°$. In Panel D, we plot τ_{odd}/H which is the sum of the orthogonal magnetization $M_\perp$ (parabolic curve) resting on a constant M_s. The sign sgn(M_s) changes with sweep direction. By contrast, sgn($M_\perp$) which identifies ω is frozen (the parabolas point "up" in both sweeps). See text.

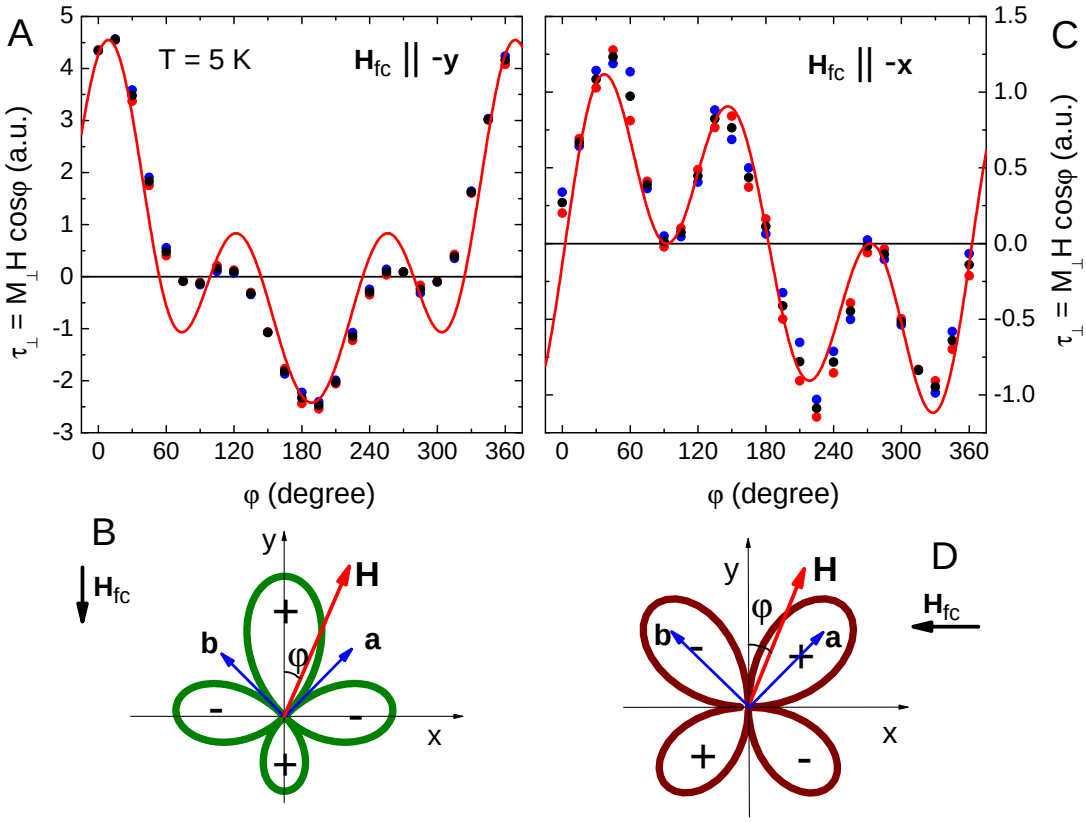

FIG. 2: The angular variation of $\tau_\perp \equiv M_\perp H \cos\varphi$ and the effect of $\mathbf{H}_{fc}$ on the d-wave orientation of $M_\perp$. Panel A displays $\tau_\perp$ vs. φ obtained after cooling in $\mathbf{H}_{fc} \parallel -\hat{\mathbf{y}}$. The red curve is the expression $M_\perp \cos\varphi \sim (1+\eta\cos\varphi)\cos 2\varphi \cdot \cos\varphi$, which fits the data well except near 90° and 270°. The curve describes the skewed d-wave pattern with lobes directed along the x and y axes (Panel B). The signs of the lobes are reversed if the sample is cooled with $\mathbf{H}_{fc}$ reversed in sign ($\parallel \hat{\mathbf{y}}$). The experiment is next repeated with $\mathbf{H}_{fc}$ rotated to $\parallel -\hat{\mathbf{x}}$. As shown in Panel C, the angular variation of $\tau_\perp$ is now different from Panel A. The data fit well to the expression $(1+\eta\cos\varphi)\sin 2\varphi \cdot \cos\varphi$. The polar representation (Panel D) shows a d-wave pattern rotated relative to B, with lobes now directed along the a and b axes. The signs of the lobes are reversed if $\mathbf{H}_{fc}$ is reversed in sign. In A and C, red (blue) symbols are data obtained in sweep-up (sweep-down) scans while black symbols indicate their average.

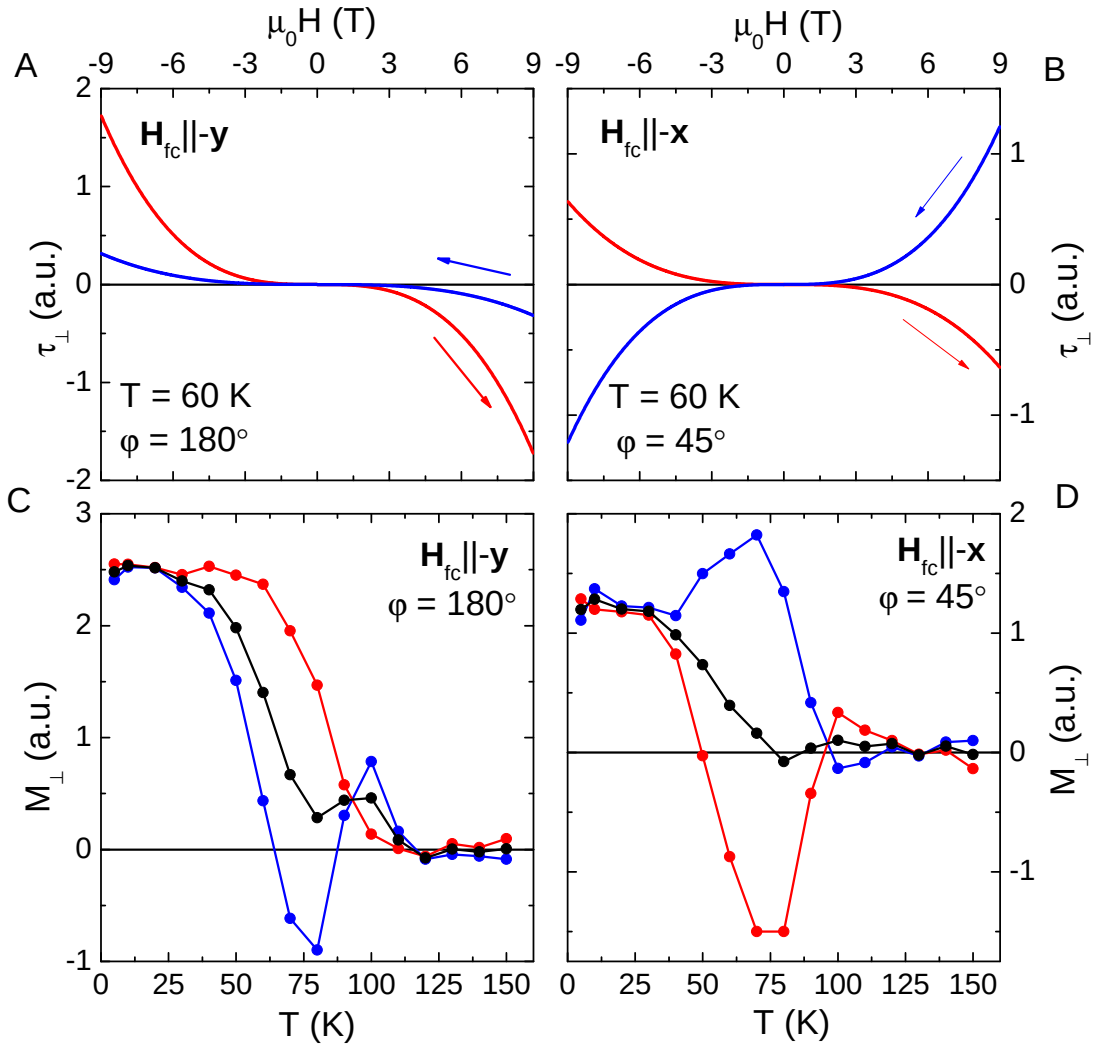

FIG. 3: The hysteretic behavior and T dependence of the nonlinear orthogonal magnetization $M_\perp$. Panel A displays curves of $\tau_\perp$ measured vs. H at T = 60 K with φ fixed at 180° (lobe direction), after cooling in $\mathbf{H}_{fc} \parallel -\hat{\mathbf{y}}$. A large hysteresis exists between the field sweep-up (-9 → 9 T, red curve) and sweep-down (9 → -9 T, blue) curves. The measurements are repeated with $\mathbf{H}_{fc} \parallel -\hat{\mathbf{x}}$. Curves measured in the new lobe direction, $\varphi = 45°$, are shown in Panel B. Panel C shows the T dependence of the nonlinear, orthogonal susceptibility $\chi_\perp \sim M_\perp/H^2$ inferred from sweep-up (red symbols) and sweep-down (blue) curves as shown in Panel A ($\mathbf{H}_{fc} \parallel -\hat{\mathbf{y}}$). Their average (black symbols) grows like an order parameter below T_N. Panel D shows the nonlinear susceptibility vs. T inferred from curves as shown in Panel B. In both C and D, the hysteresis amplitude decreases very rapidly below ∼ 80 K, becoming unresolved below 30 K.

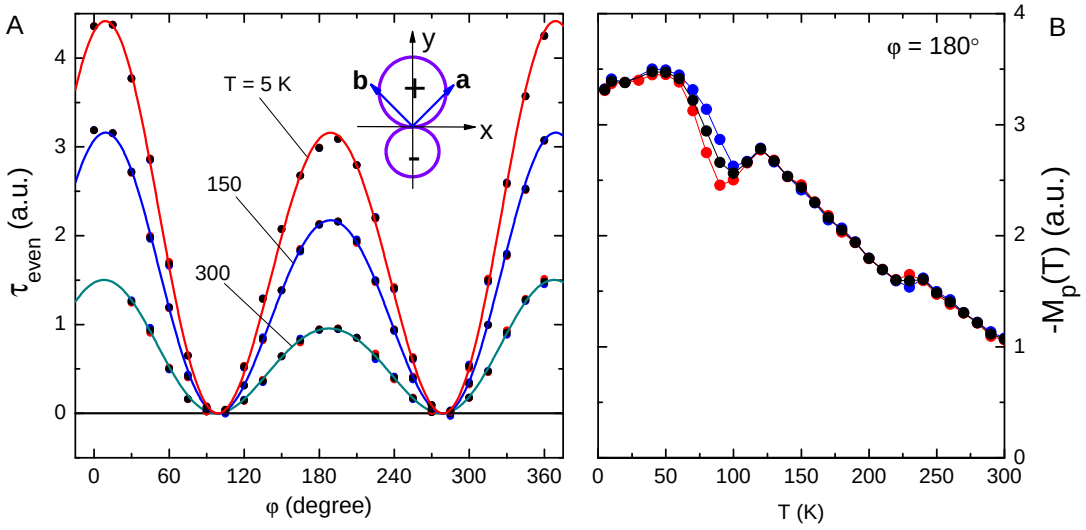

FIG. 4: The paramagnetic magnetization. Panel A shows the angular dependence of H-even component of the torque τ_{even} measured at 5, 150 and 300 K (Eq. 2). The solid curves are fits to Eq. 5. Amplitude modulation caused by the parameter η supresses the maximum at 180° relative to that at 0° (and 360°). We estimate that $\eta = 0.17$ at 5K, 0.18 at 150 K, and 0.22 at 300 K. The suppression is also apparent in the polar representation of the p-wave form in M_p shown in the inset. Panel B plots the T dependence of M_p measured at $\varphi = 180°$. M_p decreases monotonically between 50 K and 300 K, aside from a kink feature near T_N (red and blue circles are M_p measured in sweep up and sweep-down scans; black circles are the average).